Journal of Materials Chemistry A

PAPER

View Article Online
View Journal | View Issue

Cite this: J. Mater. Chem. A, 2017, 5, 9785

Novel p-type thermoelectric materials Cu_3MCh_4 (M = V, Nb, Ta; Ch = Se, Te): high band-degeneracy†

A. J. Hong,[a] C. L. Yuan,*[a] G. Gu[a] and J.-M. Liu*[bc]

Received 11th March 2017
Accepted 15th April 2017

DOI: 10.1039/c7ta02178j

rsc.li/materials-a

The good thermoelectric performance of some half-Heusler (HH) alloys has been stimulating substantial efforts in searching for more materials with similar crystal structures but better properties. In this work, we predict a new class of thermoelectric materials Cu_3MCh_4 (M = V, Nb, Ta; Ch = Se, Te) with similar lattice structures to HH alloys. The electronic and thermal transport properties of these materials are quantitatively evaluated using first-principles calculations in combination with the semi-classical transport theory. The largest *ZT* values at 1000 K for p-type Cu_3MTe_4 and Cu_3MSe_4 (M = V, Nb, Ta) can reach up to 2.06, 2.22, 2.36 and 1.91, 2.35 and 2.03, respectively. It is suggested that high band-degeneracy near the valence band edge is the main physical source for the predicted excellent thermoelectric performance. Simultaneously, a smaller effective mass of holes than that of electrons also benefits the enhanced thermoelectric properties of these p-type materials.

I. Introduction

Along with the rapid development of the world economy and growth of population, the consumption of coal, oil, and other fossil fuels is growing, which can cause the depletion of these energy sources substantially on one hand, and serious environmental pollution problems on the other hand.[1–3] More worrying is that local wars for competing energy sources are common. We must search for alternative energy sources for overcoming energy shortage.[4–6] Thermoelectric (TE) devices have special functionalities in converting waste heat into electricity and *vice versa*,[7–9] promisingly contributing to waste heat utilization and refrigeration engineering.[10–12] Therefore, TE materials have been attracting continuous attention in the past few years as well as superconducting materials and topological insulator materials.[13–19]

Technically, whether a TE material can be widely utilized in electricity generation depends on the dimensionless figure of merit (FOM) factor *ZT* which is defined by a relation $ZT = S^2\sigma T/\kappa_{tot}$,[20,21] where $S^2\sigma$ is called the power factor (PF), and S, σ, T, and κ_{tot} respectively are the TE power (also called the Seebeck coefficient), electrical conductivity, absolute temperature, and total thermal conductivity containing two contributions from the charge carriers (κ_e) and phonons (κ_L). It is clear that a material with favorable TE properties should simultaneously possess high PF and low thermal conductivity.[22–24] However, it is difficult to achieve the two targets simultaneously, as a result of the intrinsic but complex contradiction between these parameters.[25–27] From the viewpoint of energy band engineering, the necessary condition for a high Seebeck coefficient is that the top of the valence band (VB) for p-type carriers or the bottom of the conduction band (CB) for n-type carriers should be relatively flat in the momentum (k) space. On the contrary, a high electrical conductivity needs a steep band edge. Thus, it becomes quite challenging to maximize both the Seebeck coefficient and electrical conductivity if a material only has one valence band maximum (VBM) and one conduction band minimum (CBM), also called single-valley semiconductors. However, it is noted that the degeneracy of bands at the same VBM/CBM (called band convergence) or at the different VBMs/CBMs, as shown in Fig. 1(a) and (b), respectively, has been believed to be able to overcome these difficulties. In this case, a high Seebeck coefficient can be maintained by the heavy

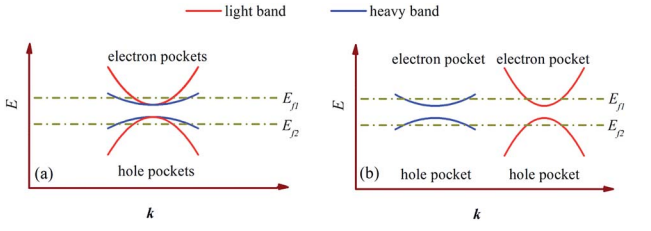

Fig. 1 The band degeneracy at the same k-point (a) and at the different k-points (b).

[a]Jiangxi Key Laboratory of Nanomaterials and Sensors, School of Physics, Communication and Electronics, Jiangxi Normal University, Nanchang 330022, China. E-mail: clyuan@jxnu.edu.cn

[b]Laboratory of Solid State Microstructures, Innovation Center of Advanced Microstructures, Nanjing University, Nanjing 210093, China. E-mail: liujm@nju.edu.cn

[c]Institute for Advanced Materials, Laboratory of Quantum Engineering and Quantum Materials, South China Normal University, Guangzhou 510006, China

† Electronic supplementary information (ESI) available. See DOI: 10.1039/c7ta02178j

bands (blue lines) at the band edges, and relatively good electrical conductivity can be obtained because the light bands (red lines) are relatively steep in shape.

Realistic materials usually have more than one VBM/CBM, as shown in Fig. 1(b), but the band degeneracy at different VBMs/CBMs rarely occurs in the strict sense since it is more than lucky to meet a case where different local VBMs/CBMs have the same energy. Fortunately, practical TE materials are more or less subjected to carrier doping or substitution, allowing a slight adjustment of the Fermi level which could level up (Fermi level E_{f1}) to cross the CBM or level down (Fermi level E_{f2}) to cross the VBM, as shown in Fig. 1. Certainly, it is better if there are more such crosses. Recently, it was indeed revealed that some materials have more than two local VBMs/CBMs, which are called multi-energy valley (MEV) semiconductors. The physics can be clearly illustrated in Fig. 1(b) as an example. The total number of electron/hole pockets depends on the number of CBMs/VBMs in the first Brillouin zone and the location of the Fermi level. More electron/hole pockets are favorable for achieving better TE properties because more conductive carriers are allowed while heavy bands maintain a high Seebeck coefficient.

The above discussion provides a clue in the search for better TE materials. The materials that have more MEVs and thus higher band-degeneracy would have more electron/hole pockets and thus should be highly considered. In fact, this argument is not new and has been confirmed from many earlier experiences. For example, p-type PbSe and PbTe have at least 12 hole pockets and n-type $CoSb_3$ skutterudites also have 12 electron pockets.[28,29] The half-Heusler (HH) compound NbFeSb has six band degenerate states at the CBM (the X point) and five additional equivalent points.[30] For NbFeSb, one finds two-fold degeneracy at the VBM, namely two energy bands converging at the point L. Since the L point for each energy band has four equivalent points in the first Brillouin zone, the total degeneracy number of the VBs is eight.[31] In this case, once the Fermi level crosses the VBs, at least eight hole-pockets would be obtained. This compound illustrates as a good example how a good TE material relies on the details of the electronic structure, and in particular how important a larger degeneracy number near the Fermi level is appreciated.

As a general scenario, a material with a high-symmetry crystal structure usually possesses high band-degeneracy, and has a high melting point which is beneficial to the application of TE materials. Certainly, a TE material for practical applications can't be a pure compound but optimally doped semiconductors with the appropriate carrier densities. This requires an easy regulation of the carrier density by doping. For example, for HH alloys, half of the position (0.25, 0.25, 0.25) and its equivalent sites in the crystal structures are filled by atoms and the other half are vacancies, which is conducive to the introduction of exotic atoms for adjusting the carrier density. Along this line, semiconductors Cu_3MCh_4 (M = V, Nb, Ta; Ch = Se, Te) with a cubic crystal structure come to our attention. Their electronic and phonon structures and TE properties will be systematically studied using first-principles calculations combined with the semi-classical transport theory. We investigate their Fermi surfaces near the top of VBs and do identify high band-degeneracy. Consequently, it is predicted that the largest ZT values at 1000 K for the p-type Cu_3MTe_4 and Cu_3MSe_4 (M = V, Nb, Ta) can reach up to 2.06, 2.22, 2.36, 1.91, 2.35 and 2.03, respectively.

II. Computational details

In this study, we use first-principles calculations within the density functional theory (DFT) framework which is implemented in the WIEN2k code and adopt the generalized gradient approximation of Perdew–Burke–Ernzerhof (GGA-PBE) to optimize the crystal structure.[32] In the calculations, the minimization of forces is set less than 1mRy/a.u. acting on each atom. The muffin-tin radii of Cu and M atoms are set to 2.0 a.u., and those of Ch atoms are set to 2.3 a.u. The plane-wave cut-off of $R_{MT}\cdot K_n = 7.0$ is used. For the calculations of the electronic structure and elastic properties, a very dense k mesh is used in order to acquire accurate results. It is noted that the normal GGA method usually underestimates the band gap, and instead the GGA modified by the Becke-Johnson (mBJ) is also implemented in calculating the electronic structure for comparison.[33] The electrical transport properties are calculated using the semi-classic Boltzmann transport theory. In this theoretical framework, the calculation of the relaxation time is critical. In our work, the deformation potential theory (DP) combining the effective mass approximation method is used to calculate the relaxation time which is described by the equations:

$$\tau = \frac{\mu m}{e}, \tag{1}$$

$$\mu = \frac{2\sqrt{2\pi}e\hbar^4 c_{ii}}{3(k_B T)^{3/2} m^{5/2} {\lambda_\beta}^2}, \tag{2}$$

where e is the unit charge, μ is the carrier mobility, $\hbar$ and k_B are the Planck constant and the Boltzmann constant, c_{ii} is the lattice elastic constant, λ_β is the DP constant, T is the absolute temperature, and m is the effective mass which can be calculated by the following equations:

$$\begin{aligned} m^*_{\alpha\beta}(\varepsilon) &= \frac{\sum_{i,k} m_{\alpha\beta}\delta(\varepsilon - \varepsilon_{i,k})}{\sum_{i,k}\delta(\varepsilon - \varepsilon_{i,k})} \\ m_\varepsilon(\varepsilon) &= \sqrt[3]{m^*_{11}(\varepsilon)\cdot m^*_{22}(\varepsilon)\cdot m^*_{33}(\varepsilon)}, \quad (\alpha = \beta = 1,2,3) \\ m &= m_\varepsilon(\varepsilon)|_{\varepsilon = E_{edge}}, \end{aligned} \tag{3}$$

where $m_{\alpha\beta}$ is the effective mass tensor at the k point with the band index i. It is seen here that the relaxation time is T-dependent in our calculations.

For the calculation of the phonon spectrum, density functional perturbation theory (DFPT) calculations are performed in the Phonopy code combined with the VASP package.[34] In order to obtain an accurate phonon spectrum, the $2 \times 2 \times 2$ supercell is used to calculate the real-space force constants, and a $7 \times 7 \times 7$ Monkhorst–Pack k-mesh in the first Brillouin-zone and the cutoff energy 400 eV are set. More details about the calculations were given in our previous studies.[31,35]

III. Results and discussion

A. Electronic structures

Structurally, Cu_3MCh_4 compounds have a high-symmetry cubic crystal structure as shown in Fig. 2 and belong to the #215 space group. This structure is very similar to that of the HH alloy NbFeSb which belongs to the #216 space group.[31] For NbFeSb, the Fe atoms fill the Wyckoff position 4c, corresponding to the fractional coordinates (0.25, 0.25, 0.25). For Cu_3MCh_4, the Ch atoms fill the position (~0.24, ~0.24, ~0.24) and its equivalent positions, very close to NbFeSb. After sufficient optimization of the lattice volume and atomic internal coordinates, the evaluated lattice constants of the six compounds are presented in Table 1 where the measured data are also inserted for the purpose of comparison. It is indicated that the calculated values are in good agreement with measured ones, and the difference between them is within the acceptable range. The differences in the calculated lattice parameters between compounds Cu_3TaCh_4 and Cu_3NbCh_4 are 0.01 Å, smaller than those between compounds Cu_3VCh_4 and Cu_3NbCh_4, which is largely due to nearly the same ionic radii of Nb and Ta.

The band structures and corresponding total and partial density of states (DOS and PDOS) of these compounds are evaluated. For a clearer presentation, we choose Cu_3MTe_4 as a representative example and the results on other systems are qualitatively similar. The DOS and PDOS for Cu_3MTe_4 are presented in Fig. 3, and the data for Cu_3MSe_4 are given in Fig. S1 of the ESI.† In our calculations, the GGA-mBJ method, comparable with the very expensive GW calculations, is used to compute the bandgaps in order to avoid underestimating the gaps. Indeed, the bandgaps calculated using the GGA-mBJ method are significantly larger than those calculated using the normal GGA method (see Table 1). Among Cu_3VCh_4, Cu_3SbCh_4, and Cu_3TaCh_4 (Ch = Te, Se), Cu_3TaCh_4 has the largest bandgap and Cu_3VCh_4 has the smallest one. In contrast, the bandgap of Cu_3MTe_4 is smaller than that of Cu_3MSe_4 although they have identical M atoms. A straightforward understanding is that the Se atom with respect to the Te atom has large electronegativity, favoring strong ionic bonding with other atoms and thus strong electron localization. For the DOS contributions near the CBM and VBM, it is found that the electronic structure near the CBM is mainly determined by the M atoms, as shown in Fig. 3(b), (d) and (f). The electronic states near the VBM are mainly attributed to Cu and Te atoms and the contributions of the M atoms are nearly negligible, while the Ch and Cu atoms have almost the same contribution, as shown in Fig. 3(b), (d) and (f) too.

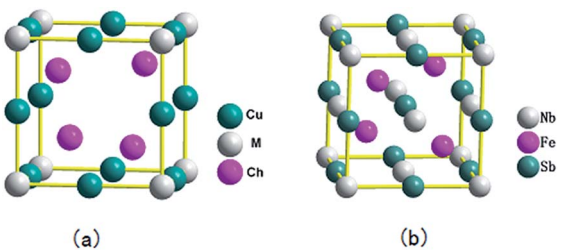

Fig. 2 Schematic drawing of the lattice structures of compounds Cu_3MCh_4 (a) and NbFeSb (b).

Table 1 Calculated (cal.) and measured (exp.) lattice constant *a* of compounds Cu_3MCh_4 (M = V, Nb, Ta; Ch = Se, Te), and bandgaps obtained using GGA-PBE and GGA-mBJ

	a (Å)		Bandgap (eV)	
Compounds	(cal.)	(exp.)	(PBE)	(mBJ)
Cu_3VTe_4	5.95	—	0.592	0.769
Cu_3NbTe_4	6.00	5.92 (ref. 36)	0.976	1.086
Cu_3TaTe_4	6.01	5.93 (ref. 37)	1.171	1.323
Cu_3VSe_4	5.65	5.57 (ref. 38)	0.829	1.061
Cu_3NbSe_4	5.73	5.65 (ref. 38)	1.376	1.520
Cu_3TaSe_4	5.74	5.67 (ref. 37)	1.611	1.828

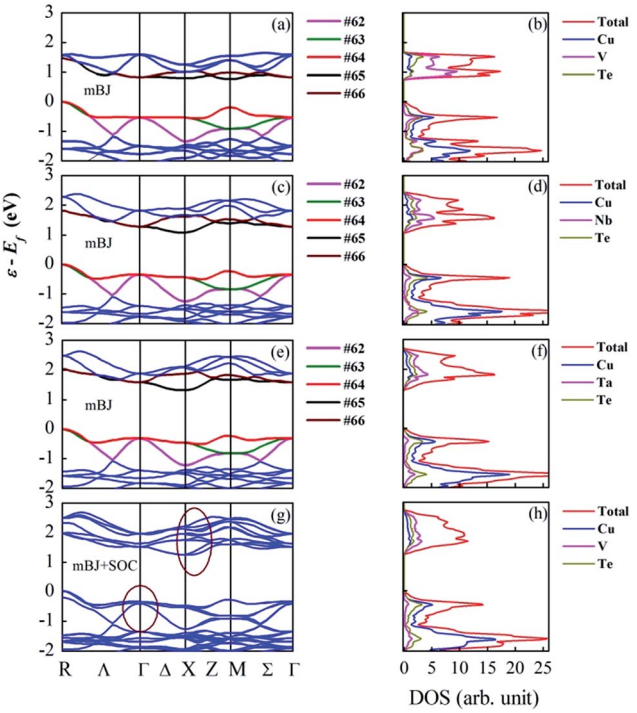

Fig. 3 The calculated band structures of Cu_3VTe_4 (a), Cu_3NbTe_4 (c), and Cu_3TaTe_4 (e) without SOC, and Cu_3TaTe_4 (g) with SOC, as well as the calculated total and partial DOS data of Cu_3VTe_4 (b), Cu_3NbTe_4 (d), and Cu_3TaTe_4 (f) without SOC, and Cu_3TaTe_4 (g) with SOC.

Our major concern is about the band degeneracy of the electronic structure of these compounds. Again, one takes Cu_3MTe_4 as an example for illustration and the others show similar characters. We see the two-fold degeneracy of the CBs and three-fold degeneracy of the VBs at the Γ point. The two-fold degeneracy includes two CBs (labeled as #65 and #66), and the three-fold degeneracy includes #62, #63, and #64 VBs. Another three-fold degeneracy containing the #62, #63 and #64 VBs occurs at the *R* point (VBM), and they overlap near the Γ and *R* points. In particular, the #63 and #64 VBs overlap along the high symmetry points. This band-overlap especially at the CBM/VBM benefits the TE performance a lot, because it

contains both the heavy bands and light bands, as discussed earlier.

It is known that the spin–orbit coupling (SOC) effect in materials containing heavy elements (such as the sixth period elements) is no longer negligible. This effect could be significant too in two-dimensional materials, which may induce band inversion and band splitting. However, the calculations including the SOC usually require a huge amount of computing resources, and much more would be required in the mBJ if the SOC is included. In order to evaluate how important the SOC effect on energy bands in the compounds is and save computational resources, our strategy is to choose one member of the compound family here, and this member may exhibit the strongest SOC effect on the band structure. Here, we choose the compound Cu_3TaTe_4 which contains heavy elements Te and Ta. The calculated band structures, and total and partial DOS including SOC, are shown in Fig. 3(g) and (h). It is seen that the SOC leads to band splitting occurring at many k points, as shown in Fig. 3(g). However, the bandgap and the shape of the VBM and CBM show only a weak response to the SOC. The calculated bandgap is 1.294 eV if the SOC is considered, slightly smaller than 1.323 eV if the SOC is excluded. The effective masses are 0.32 m_e and 2.05 m_e at the VBM and CBM, which are only slightly different from those without the SOC. It is known that the TE properties are mainly decided by the bandgap and the effective masses at the VBM and CBM. Our results on the SOC effect in Cu_3TaTe_4 suggest that the SOC effect on our compound family Cu_3MCh_4 should be weak if any, in terms of its influence on the TE properties.

It is known that the TE properties of a compound depend also on the carrier type. The p-type Cu_3MTe_4 shows high band-degeneracy at the VBM, possibly allowing good TE properties. To check this prediction, one may discuss in detail the Fermi surfaces, and here we focus on the p-type Cu_3VTe_4. The Fermi surfaces for the #62, #63, and #64 VBs are calculated and plotted in Fig. 4. The light-blue shaded area represents the first Brillouin zone and the Γ point is set to the zone center. The Fermi surfaces for the VBs are composed of eight identical surface sections located near the vertices (R point and its seven equivalent points) of the reciprocal cell. The shape of the Fermi surface for the #64 VB is almost a sphere. The Fermi surface for the #63 VB looks like a pseudo cube but there is an arch-like feature on each face of the pseudo cube, and it is noted that the reciprocal a^*, b^*, c^* axes along the three central axes of the pseudo cube pass through these arch faces respectively. Very different from the 63 VB, the #62 VB has a polyhedron-like Fermi surface composed of three ellipsoids perpendicular to each other. The a^*-, b^*-, and c^*-axes align along the major axes of three ellipsoids in the polyhedron.

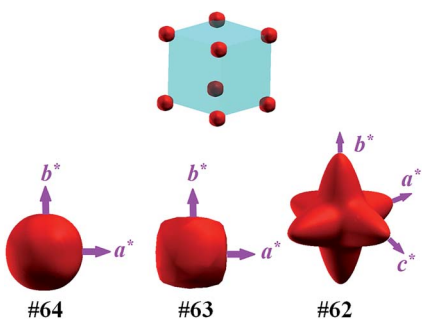

Fig. 4 Fermi surfaces at the energy level of 0.136 eV below the VBM for the VBs #64, #63 and #62.

Now we discuss the effect of these Fermi surfaces on the TE properties. The electrical transport is mainly determined by the electronic structure near the VBMs and CBMs whereas the Fermi level is inside the bandgap. Since the three VBs, #62, #63, and #64, have very different Fermi surface geometries, the effective masses are different. The spherical Fermi surface for the #64 VB is trivial and the effective mass is spatially isotropic and also small. For the #63 VB, the shapes near the intersection points with the reciprocal axes exhibit big curvatures, leading to relatively large effective masses. For the #62 VB the Fermi surface local geometry shows the biggest curvatures along the main axes, and thus the largest effective masses. Given the identification of heavy and light bands as well as the relationships of the effective mass against the electrical conductivity and Seebeck coefficient mentioned above, the electrical conductivity can be remarkably enhanced due to the small effective mass associated with the light bands, while the Seebeck coefficient can be high too due to the big curvature of the heavy bands.

B. Phonon structures

A suitable phononic structure is also critical for optimizing the TE properties of a compound. Our calculations show that these compounds have qualitatively similar phononic structures and we tentatively choose Cu_3VTe_4 as an example for details. The unit cell of Cu_3MCh_4 has eight atoms made up of three Cu atoms, one M atom, and four Ch atoms. Therefore, Cu_3MCh_4 has in total 24 phononic branches, as shown in Fig. 5 and S2 of the ESI,† which consist of 21 optical branches and 3 acoustic branches. It is noted that the long-wavelength acoustic branches must converge at the Γ point and the two transverse acoustic (TA) branches overlap over almost the whole region. Also, we find that one TA branch deviates from the other one along the Z–M–Σ direction and overlaps with the longitudinal acoustic (LA) branches. As is known, the phonon bandgap is conducive to reduce phonon scattering. In particular, the bandgap between the acoustic branch and optical branch is harmful to obtain a low lattice thermal conductivity. Fortunately, there are many overlaps along the high symmetry lines between the acoustic branch and optical branch. Simultaneously, here the phonon energy of the acoustic branches is not high. The highest frequency of the acoustic branches is ~1.7 THz, much lower than 5.6 THz of HH NbFeSb. Since the lattice thermal conductivity is mainly attributed to the vibration of acoustic branches, the low phonon energy for these acoustic branches suggests that phonons carry low energy during the heat transport, favorable for a low lattice thermal conductivity.

The calculated total and partial phonon DOS of the Cu_3VTe_4 and Cu_3VSe_4 are plotted in Fig. 5(b), (d) and (f), as well as in

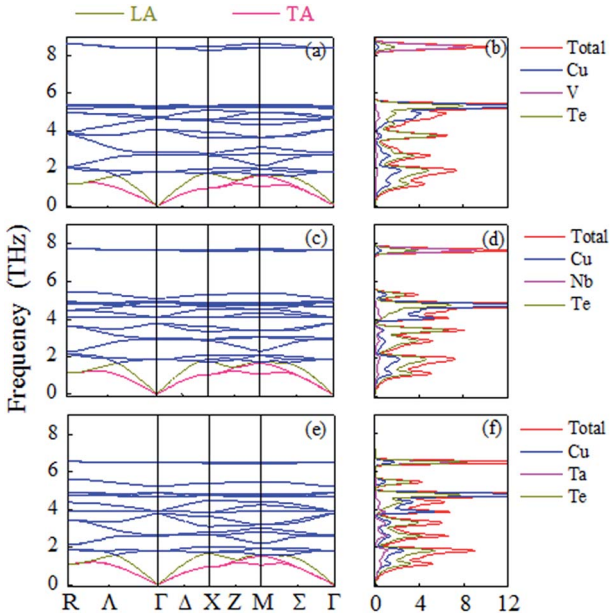

Fig. 5 The calculated phonon spectra of Cu_3VTe_4 (a), Cu_3NbTe_4 (c), and Cu_3TaTe_4 (e), and the calculated total and partial phonon DOS data of Cu_3VTe_4 (b), Cu_3NbTe_4 (d), and Cu_3TaTe_4 (f).

Fig. S2(b), (d) and (f) in the ESI.† It is clear that the vibrations of the Ch atoms are the main source of low-frequency acoustic branches and those of the M atoms are fairly weak. This suggests that an appropriate doping at the Ch-site would be effective in reducing the lattice thermal conductivity.

C. Elastic properties and electrical transport

Besides the electronic and phononic structures, the elastic property of a material is also one of the ingredients for determining the carrier and phonon transport. The carrier mobility is directly related to the principal elastic coefficients c_{ii}, according to the deformation potential theory (DP). The Debye temperature Θ_D and Grüneisen parameter γ related to the bulk modulus B and shear modulus G also have crucial influence on lattice thermal conductivity κ_L. Compounds Cu_3MCh_4, which have the cubic crystal structure, possess three independent elastic coefficients (c_{11}, c_{12} and c_{14}). The calculated elastic parameters for the six materials are summarized in Table 2. It is clear that the elastic coefficients c_{ii} are larger than c_{ij}, and correspondingly, the bulk modulus B is larger than the shear modulus G for all the materials, indicating that the G/B ratios are smaller than unity and the materials are not very fragile. This is favorable in terms of TE performance. Poisson's ratios ν for these materials are also listed in Table 2. All these values are low and not very different, suggesting that the materials have small deformation perpendicular to the stretching/compression direction. The B and G values are quite smaller than $B = 163.62$ GPa and $G = 63.04$ GPa of the HH NbFeSb alloy,[31] implying that the Cu_3MCh_4 would have lower Θ_D but high melting points.

Furthermore, a set of relevant parameters for evaluating the TE properties, *i.e.* the DP constant γ, effective mass m, mobility μ, and relaxation time τ at temperature $T = 300$ K for the n-type and p-type Cu_3MCh_4, are calculated and summarized in Table 3. It is noted that the DP constants of the VBM/CBM are calculated using the average electrostatic potential in the plane which contains the Cu site and is perpendicular to the tensile direction as the reference energy levels.[39] All the λ values are not quite different from each other and smaller than that of the HH FeNbSb alloy. A small λ implies a weak electron–phonon interaction that benefits the high electrical conductivity. Another physical parameter which has an important influence on the electrical transport is the effective mass of the VBM/CBM. Generally, the effective mass m_p of the holes for most semiconductors is higher than the effective mass m_n of the electrons. The calculated effective mass m_p of holes for compounds Cu_3MCh_4 is smaller than the effective mass m_n of electrons. The compound Cu_3VSe_4 has its electron effective mass $m_n \sim 3.47m_e$, which is ~6.5 times heavier than m_p ~$0.46m_e$, where m_e is the electron mass. This unusual fact is due to the strong Cu-3d and Se-4p hybridization. As is known, one closed shell is composed of $3d^{10}$ electrons in the Cu cation and can strongly hybridize with chalcogen p electrons, which lowers the chalcogen character and leads to the wide dispersion of the valence band with small effective mass.[40] Reasonably, the difference in effective mass between the p-type and n-type carriers will lead to a big difference in mobility. This is the reason why all the mobility values for the p-type Cu_3MTe_4 and

Table 2 The calculated elastic constants c_{11}, c_{12}, and c_{44}, bulk modulus B and shear modulus G (in units of GPa), as well as Poisson's ratio ν of Cu_3MCh_4 (M = V, Nb, Ta; Ch = Se, Te)

Compounds	c_{11}	c_{12}	c_{44}	B	G	ν
Cu_3VTe_4	86.59	47.35	53.42	60.43	35.76	0.25
Cu_3NbTe_4	94.26	47.84	52.50	63.31	37.83	0.25
Cu_3TaTe_4	93.81	50.82	53.69	65.15	37.19	0.26
Cu_3VSe_4	109.52	52.83	57.80	71.73	43.42	0.24
Cu_3NbSe_4	116.31	52.25	53.45	73.60	43.52	0.25
Cu_3TaSe_4	116.44	55.89	54.87	76.08	43.22	0.26

Table 3 The calculated DP constant λ (in units of eV), effective mass m (in units of m_e), mobility μ (in units of $cm^2\ V^{-1}\ s^{-1}$), and relaxation time τ (in units of fs) at $T = 300$ K for the n-type and p-type Cu_3MCh_4 (M = V, Nb, Ta; Ch = Se, Te), respectively. m_e is the mass of an electron

Compounds	λ	m	μ	τ
p-type				
Cu_3VTe_4	−9.99	0.34	550.3	106.5
Cu_3NbTe_4	−10.08	0.35	526.7	104.9
Cu_3TaTe_4	−10.09	0.34	580.4	112.3
Cu_3VSe_4	−9.44	0.46	343.5	89.9
Cu_3NbSe_4	−9.40	0.41	473.0	110.4
Cu_3TaSe_4	−9.40	0.51	283.3	82.2
n-type				
Cu_3VTe_4	−10.11	1.96	6.7	7.5
Cu_3NbTe_4	−10.06	1.89	7.8	8.4
Cu_3TaTe_4	−9.92	2.03	6.9	7.9
Cu_3VSe_4	−10.14	3.47	1.9	3.7
Cu_3NbSe_4	−9.02	1.58	17.6	15.8

Cu_3MSe_4 are two orders of magnitude larger than that for the n-type compounds. The calculated relaxation time for the p-type Cu_3MTe_4 and Cu_3MSe_4 at 300 K is ~100 fs which is larger than that of typical semiconductors (~10 fs). This is mainly due to the effects from grain boundaries, impurities, *etc.* on the relaxation time which are neglected in our calculations, but these effects could be significant in realistic polycrystalline materials.

Given the values of all these parameters, the TE properties, including S, σ, PF, and κ_e for the p-type and n-type Cu_3MCh_4 at $T = 300$ K and carrier density $n = 10^{20}$ cm^{-3} can be calculated and the data are given in Table 4. All the $|S|$ values for the n-type are larger than those for the p-type but the σ values for the n-type are smaller than those for the p-type. The PF values for the n-type are very low, and especially the PF values of Cu_3NbTe_4, Cu_3TaTe_4, and Cu_3NbSe_4 are lower than 1.0 mW m^{-1} K^2. Such a low PF is not preferred for practical applications. Fortunately, the PF for the p-type is higher than 10, yet lower than that of HH NbFeSb alloys. The advantage lies in that these compounds have low κ_e with respect to HH NbFeSb.

D. Lattice thermal transport and TE performance

The calculated Θ_D, γ, and κ_L at $T = 300$ K and 1000 K are listed in Table 5. A high Θ_D and a large γ separately describe big binding forces between atoms and weak anharmonic vibrations. A low lattice thermal conductivity requires a low Θ_D and a large γ. However, the evaluated γ values for the six compounds are yet lower than 2.0, suggesting that they have weak anharmonic vibrations, unfavorable for obtaining a low κ_L. Fortunately, these Cu_3MCh_4 compounds have sufficiently low Θ_D and the unit cell has a higher atom number than that of the compound NbFeSb and thus possesses lower κ_L. For example, the κ_L of Cu_3VTe_4 is slightly higher than 6.0 W K^{-1} m^2 at 300 K, and for the other five materials it is lower than 6.0 W K^{-1} m^2 which is about a third of ~18.0 W K^{-1} m^2 for the HH alloy NbFeSb.[26] The difference in κ_L between Cu_3NbTe_4 and Cu_3TaTe_4 is small, while that between Cu_3VTe_4 and Cu_3NbTe_4 is relatively large. The close correlation of κ_L with the lattice parameter is demonstrated in this work.

Finally, we come to evaluate the TE properties of these compounds under the optimized conditions. Usually, optimized properties such as the largest ZT values are obtained *via* carrier doping, microstructuring, and so on. Adjusting the carrier density is a convenient and effective method to enhance the PF and ZT, and the carrier density n is used as a variable for an experimental approach. We calculate these TE properties including ZT and PF as a function of T and n over a sufficiently broad (n, T) region, as plotted in Fig. 6 and S3.† Bright and dark areas separately represent the large and small ZT regions. It is clear that the p-type Cu_3TaTe_4 has the best TE performance in terms of ZT and the bright area is big, suggesting that this compound, upon appropriate carrier doping, can be utilized

Table 4 The calculated S (in units of μV K^{-1}), σ (in units of 10^5 S m^{-1}), PF (in units of mW m^{-1} K^2), and κ_e (in units of W K^{-1} m^2) separately for the n-type and p-type Cu_3MCh_4 (M = V, Nb, Ta; Ch = Se, Te)

Compounds	S	σ	PF	κ_e
p-type				
Cu_3VTe_4	172	4.46	13.32	2.73
Cu_3NbTe_4	166	4.22	11.68	2.55
Cu_3TaTe_4	167	4.45	12.53	2.71
Cu_3VSe_4	213	2.75	12.61	1.62
Cu_3NbSe_4	211	3.12	14.00	1.85
Cu_3TaSe_4	211	2.31	10.37	1.37
n-type				
Cu_3VTe_4	−336	92.94	1.05	0.04
Cu_3NbTe_4	−221	1.99	0.97	0.11
Cu_3TaTe_4	−216	2.02	0.94	0.11
Cu_3VSe_4	−322	33.43	0.34	0.01
Cu_3NbSe_4	−231	3.31	1.77	0.18
Cu_3TaSe_4	−228	4.47	2.32	0.25

Table 5 The calculated Debye temperature Θ_D (in units of K), lattice thermal conductivity κ_L (in units of W K^{-1} m^2) at 300 K and 1000 K, and Grüneisen parameter γ for Cu_3VTe_4 (M = V, Nb, Ta; Ch = Se, Te), respectively

	Θ_D			κ_L	
Compounds	300 K	1000 K	γ	300 K	1000 K
Cu_3VTe_4	291	301	1.71	6.03	1.99
Cu_3NbTe_4	269	280	1.70	5.10	1.71
Cu_3TaTe_4	252	262	1.62	5.18	1.73
Cu_3VSe_4	345	356	1.70	7.18	2.36
Cu_3NbSe_4	315	326	1.71	5.89	1.94
Cu_3TaSe_4	298	308	1.69	5.84	1.92

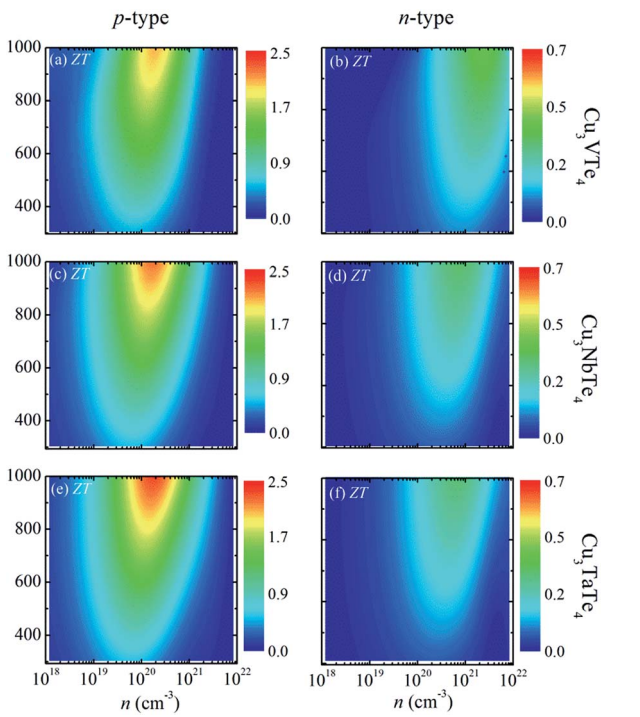

Fig. 6 The T- and n-dependences of ZT values for the p-type Cu_3VTe_4 (a), Cu_3NbTe_4 (c), Cu_3NbTe_4 (e), and for the n-type Cu_3VTe_4 (b), Cu_3NbTe_4 (d), Cu_3NbTe_4 (f).

over a broad (T, n) region. All the values of the ZTs for the n-type Cu_3MTe_4 are lower than unity, which implies that they are not good TE materials.

We extract the optimal carrier densities n_{opt} and corresponding ZT values at 300 K and 1000 K from Fig. 6 and S3 (ESI†) and the data are summarized in Table 6. It is clear that the largest ZT values of the p-type Cu_3MTe_4 (M = V, Nb, Ta) at 1000 K respectively achieve 2.06, 2.22, and 2.36, which are obviously larger than corresponding values for the n-type compounds. It is noted that the ZT values of neither n-type nor p-type compounds at 300 K are larger than unity, implying that they are not suitable for applications at room temperature. All the n_{opt} values at 1000 K for the p-type compounds are on the order of magnitude of 10^{20} cm^{-3}, which are higher than those for the n-type compounds at 300 K. In general, each of six materials has higher n_{opt} for the n-type compounds than that for the p-type ones at the same temperature.

Last but not least, it should be mentioned that the compounds addressed in this work usually have relatively large bandgaps, and this character should be discussed. It is noted that an appropriate bandgap, neither very large nor too narrow, is important for enhanced performance of a thermoelectric material. A small bandgap can lead to a strong bipolar effect which is detrimental to thermoelectric properties. A large bandgap is harmful to sufficient conductivity due to the low carrier density, although materials with large bandgaps usually have larger ZT values, given the optimal carrier density, according to previous theoretical calculations. This inspires us to investigate candidate materials with relatively large intrinsic bandgaps (without any doping). One may be able to arrange appropriate carrier doping of these materials in order to optimize the TE properties, in particular the ZT values. Surely, such a doping trial could be critical and an inappropriate doping may over-reduce the bandgap and damage the TE properties. So a general strategy along this line is highly favorable but also challenging.

Table 6 The calculated ZT values and corresponding optimal carrier densities n_{opt} (in units of 10^{19} cm^{-3} for p-type at 300 K and 10^{20} cm^{-3} for the others) at 300 K and 1000 K for Cu_3MCh_4 (M = V, Nb, Ta; Ch = Se, Te)

	300 K		1000 K	
Compounds	ZT	n_{opt}	ZT	n_{opt}
p-type				
Cu_3VTe_4	0.46	6.91	2.06	1.90
Cu_3NbTe_4	0.48	6.30	2.22	1.73
Cu_3TaTe_4	0.50	6.32	2.36	1.91
Cu_3VSe_4	0.43	12.02	1.91	3.02
Cu_3NbSe_4	0.54	10.96	2.35	3.31
Cu_3TaSe_4	0.43	12.03	2.03	4.36
n-type				
Cu_3VTe_4	0.09	9.12	0.39	27.54
Cu_3NbTe_4	0.06	2.75	0.32	8.31
Cu_3TaTe_4	0.06	2.29	0.31	7.58
Cu_3VSe_4	0.02	8.31	0.09	30.20
Cu_3NbSe_4	0.10	2.51	0.41	6.91
Cu_3TaSe_4	0.12	2.29	0.63	6.91

IV. Summary

In summary, in the light of highly favorable benefits of high band-degeneracy to the TE performance, we have predicted a class of copper-based TE compounds Cu_3MCh_4 (M = V, Nb, Ta; Ch = Se, Te) with a cubic crystal structure. The calculations suggest that their largest ZT values at 1000 K for the p-type Cu_3MTe_4 and Cu_3MSe_4 (M = V, Nb, Ta) can reach up to 2.06, 2.22, 2.36, 1.91, 2.35 and 2.03, respectively. It is revealed that the high band-degeneracy at the VBM and light effective mass for holes are the main physical reasons for the large ZT values of the p-type Cu_3MTe_4 and Cu_3MSe_4 (M = V, Nb, Ta). The low Θ_D and big atomic number in the unit cell are important reasons, also. However, the heavy effective mass of electrons may lead to relatively small ZT values for the p-type systems. In this work, the phonon and electronic structures are studied in detail and all the TE parameters have been calculated using first-principles calculations combined with the semi-classical transport theory. Based on the calculations, we obtain the optimal carrier densities for the six compounds and it is suggested that doping at the Ch-site may reduce the lattice thermal conductivity, which are valuable for practical applications.

Acknowledgements

This work is supported by the National Key Research Program of China (Grant No. 2016YFA0300101), the National Natural Science Foundation of China (Grant No. 51431006), the Science and Technology Research Project of Department of Education of Jiangxi province (Grant No. 160340), and the Open Fund of Jiangxi Key Laboratory of Nanomaterials and Sensors (Grant No. 1700001).

Notes and references

1 H. Ohta, K. Sugiura and K. Koumoto, *Inorg. Chem.*, 2008, **47**, 8429.
2 L. D. Chen, Z. Xiong and S. Q. Bai, *J. Inorg. Mater.*, 2010, **25**, 561.
3 J. S. Sakamoto, H. Schock, T. Caillat, J. P. Fleurial, R. Maloney, M. Lyle, T. Ruckle, E. Timm and L. Zhang, *Sci. Adv. Mater.*, 2011, **3**, 621.
4 S. Krishnan, N. K. Karri, P. K. Gogna, J. R. Chase, J. P. Fleurial and T. J. Hendricks, *J. Electron. Mater.*, 2012, **41**, 1622.
5 S. Chen and Z. F. Ren, *Mater. Today*, 2013, **16**, 387.
6 Y. X. Zhao, J. S. Dyck and C. Burda, *J. Mater. Chem.*, 2011, **21**, 17049.
7 R. X. Fei, A. Faghaninia, R. Soklaski, J. A. Yan, C. Lo and L. Yang, *Nano Lett.*, 2014, **14**, 6393.
8 B. Zhan, J. L. Lan, Y. C. Liu, J. X. Ding, Y. H. Lin and C. W. Nan, *J. Inorg. Mater.*, 2014, **29**, 237.

9 L. D. Zhao, S. H. Lo, Y. S. Zhang, H. Sun, G. J. Tan, C. Uher, C. Wolverton, V. P. Dravid and M. G. Kanatzidis, *Nature*, 2014, **508**, 373.
10 W. F. Li, G. Yang, J. W. Zhang and Z. W. Hou, *Eur. Phys. J. B*, 2015, **88**, 330.
11 W. S. Liu, Q. Jie, H. S. Kim and Z. F. Ren, *Acta Mater.*, 2015, **87**, 357.
12 A. Banik, U. S. Shenoy, S. Saha, U. V. Waghmare and K. Biswas, *J. Am. Chem. Soc.*, 2016, **138**, 13068.
13 J. Shuai, Z. H. Liu, H. S. Kim, Y. M. Wang, J. Mao, R. He, J. H. Sui and Z. F. Ren, *J. Mater. Chem. A*, 2016, **4**, 4312.
14 J. Y. Wang, M. Gu, Y. F. Bao, X. Y. Li and L. D. Chen, *J. Electron. Mater.*, 2016, **45**, 2274.
15 B. Wiendlocha, K. Kutorasinski, S. Kaprzyk and J. Tobola, *Scr. Mater.*, 2016, **111**, 33.
16 L. J. Zhang, J. L. Wang, Z. X. Cheng, Q. Sun, Z. Li and S. X. Dou, *J. Mater. Chem. A*, 2016, **4**, 7936.
17 L. D. Zhao, G. J. Tan, S. Q. Hao, J. Q. He, Y. L. Pei, H. Chi, H. Wang, S. K. Gong, H. B. Xu, V. P. Dravid, C. Uher, G. J. Snyder, C. Wolverton and M. G. Kanatzidis, *Science*, 2016, **351**, 141.
18 J. Mao, Z. H. Liu and Z. F. Ren, *npj Quantum Materials*, 2016, **1**, 16028.
19 M. S. Scheurer, D. F. Agterberg and J. Schmalian, *npj Quantum Materials*, 2017, **2**, 9.
20 F. Hao, P. F. Qiu, Y. S. Tang, S. Q. Bai, T. Xing, H. S. Chu, Q. H. Zhang, P. Lu, T. S. Zhang, D. D. Ren, J. K. Chen, X. Shi and L. D. Chen, *Energy Environ. Sci.*, 2016, **9**, 3120.
21 Q. H. Zhang, X. Y. Huang, S. Q. Bai, X. Shi, C. Uher and L. D. Chen, *Adv. Eng. Mater.*, 2016, **18**, 194.
22 A. T. Duong, V. Q. Nguyen, G. Duvjir, V. T. Duong, S. Kwon, J. Y. Song, J. K. Lee, J. E. Lee, S. Park, T. Min, J. Lee, J. Kim and S. Cho, *Nat. Commun.*, 2016, **7**, 13713.
23 D. Wu, S. Z. Huang, D. Feng, B. Li, Y. X. Chen, J. Zhang and J. Q. He, *Phys. Chem. Chem. Phys.*, 2016, **18**, 23872.
24 H. Zhang, Y. M. Wang, K. Dahal, J. Mao, L. H. Huang, Q. Y. Zhang and Z. F. Ren, *Acta Mater.*, 2016, **113**, 41.
25 N. Miyazaki, N. Adachi, Y. Todaka, H. Miyazaki and Y. Nishino, *J. Alloys Compd.*, 2017, **691**, 914.
26 C. G. Fu, S. Q. Bai, Y. T. Liu, Y. S. Tang, L. D. Chen, X. B. Zhao and T. J. Zhu, *Nat. Commun.*, 2015, **6**, 8144.
27 C. Melnick and M. Kaviany, *Phys. Rev. B: Condens. Matter Mater. Phys.*, 2016, **94**, 245412.
28 Y. L. Tang, Z. M. Gibbs, L. A. Agapito, G. Li, H. S. Kim, M. B. Nardelli, S. Curtarolo and G. J. Snyder, *Nat. Mater.*, 2015, **14**, 1223.
29 Y. Z. Pei, X. Y. Shi, A. LaLonde, H. Wang, L. D. Chen and G. J. Snyder, *Nature*, 2011, **473**, 66.
30 W. Li, G. F. Yang and J. W. Zhang, *J. Phys. D: Appl. Phys.*, 2016, **49**, 195601.
31 A. J. Hong, L. Li, R. He, J. J. Gong, Z. B. Yan, K. F. Wang, J. M. Liu and Z. F. Ren, *Sci. Rep.*, 2016, **6**, 22778.
32 K. Schwarz, P. Blaha and G. K. H. Madsen, *Comput. Phys. Commun.*, 2002, **147**, 71.
33 A. D. Becke and E. R. Johnson, *J. Chem. Phys.*, 2006, **124**, 221101.
34 S. Baroni, S. de Gironcoli, A. Dal Corso and P. Giannozzi, *Rev. Mod. Phys.*, 2001, **73**, 515.
35 A. J. Hong, J. J. Gong, L. Li, Z. B. Yan, Z. F. Ren and J. M. Liu, *J. Mater. Chem. C*, 2016, **4**, 3281.
36 G. E. Delgado, A. J. Mora, P. Grima-Gallardo, S. Duran, M. Munoz and M. Quintero, *Chalcogenide Lett.*, 2009, **6**, 335.
37 J. Li and H. Y. Guo, *J. Solid State Chem.*, 1995, **117**, 247.
38 A. E. Van Arkel and C. Crevecoeur, *J. Less-Common Met.*, 1964, **5**, 177.
39 K. Nakamura, S. Yamada and T. Ohnuma, *Mater. Trans.*, 2013, **54**, 276.
40 G. Hautier, A. Miglio, G. Ceder, G. M. Rignanese and X. Gonze, *Nat. Commun.*, 2013, **4**, 2292.

